A Depth From Defocus Measurement System Using a Liquid Lens Objective for Extended Depth Range

Simone Pasinetti, Ileana Bodini, Matteo Lancini, Franco Docchio, and Giovanna Sansoni

***Abstract*— A novel depth from defocus (DFD) measurement system is presented, where the extension of the measurement range is performed using an emergent technology based on liquid lenses. A suitable set of different focal lengths, obtained by properly changing the liquid lens supply voltage, provides multiple camera settings without duplicating the system elements or using moving parts. A simple and compact setup, with a single camera/illuminator coaxial assembly, is obtained. The measurement is based on an active DFD technique using modulation measurement profilometry for the estimation of the contrast at each image point as a function of the depth range. Two different measurement methods are proposed, both based on a combination of multiple contrast curves, each derived at a specific focal length. In the first method (intensity contrast method), the depth information is recovered directly from the contrast curves, whereas in the second (differential contrast method), the depth is measured using contrast curve pairs. We obtained a measurement σ_0 of 0.55 mm over a depth range of 60 mm with the intensity contrast method (0.92% of the total range) and an σ_0 of 0.76 mm over a depth range of 135 mm with the differential contrast method (0.56% of the total range). Thus, the intensity contrast method is within the state-of-the-art DFD systems, whereas the differential contrast method allows, σ_0 being almost equal, a remarkable extension of the depth range.**

***Index Terms*— Calibration, image edge analysis, image processing, lenses, phase modulation, shape measurement.**

I. Introduction

3-D PROFILOMETRY plays a fundamental role in a number of applications, such as automated inspection manufacturing, reverse engineering, virtual reality, cultural heritage, and medicine [1]–[5]. A number of measuring systems were developed to measure 3-D shapes, including stereo vision [6], [7]. Active stereo vision is of major interest due to its robustness and accuracy: a number of layouts based on the projection of structured patterns were studied and engineered over the years, leading to a wide offer of market available devices. However, the optical triangulation layout requires a point to be visible in two angles, leading to occlusions, which remains a challenging problem for complex objects.

Monocular systems based on pseudo-stereo layouts [8], [9] and coaxial 3-D measurement techniques remove this limitation. Among them, systems based on depth from defocus (DFD) methods are being widely studied [10], [11]. A considerable number of measurement setups were proposed over the years, based on both passive and active illumination. Passive systems rely on the scene illumination, and derive the depth information from the analysis of the contrast of the image edges. They are attractive in terms of simplicity of the optical layout; however, they require that the scene is suitably illuminated and sufficiently texturized [12]. In addition, the processing is computationally complex [13]. Active DFD systems overcome these limitations: structured light patterns are projected on the scene, and the depth information is retrieved by analyzing the contrast changes exhibited by the patterns associated with the local depth variations [14]. In [15] and [16], sinusoidal pattern projection was proposed, combined to modulation measuring profilometry (MMP) to obtain the contrast curves. Through calibration, contrast curves can be correlated with depth information.

Both passive and active DFD systems inherently suffer from a limited measurement range: in fact, due to the "bell-like" shape of the contrast curves, it is impossible to distinguish whether the defocus plane is in front or behind the in-focus plane. Thus, only one half of the contrast curves can be used to obtain unambiguous depth measurements. In the literature, the extension of the measurement range is achieved by duplicating either the projection or the acquisition system devices.

For example, in [17], two cameras acquire different contrast curves, and the monotonic rising side of the former is combined with the monotonic falling side of the latter to extend the measurement range. An alternative approach is proposed in [18] and [19], where two sinusoidal gratings oriented perpendicularly to each other are projected on the scene and imaged on a single camera. The gratings are focused at different distances from the lens image plane, resulting in a pair of partially overlapped contrast curves. As in [17], the monotonic sides of the two contrast curves are used to compute the depth information. The above-mentioned methods yield the maximum measurement ranges of about 70 mm, with depth errors from 0.7% to 1.6% of the range. An alternative approach to the extension of the depth range is represented by time-multiplexing some of the optical components of the measurement system, in the projection and/or detection scheme. One of the possible solutions is using motor-driven optical zooms in the camera or in the projector, which replace the multicamera or multipattern approach, as proposed in [20].

In this paper, a novel DFD measurement system is presented, where the extension of the measurement range is performed using an emergent technology based on liquid

Manuscript received November 16, 2016; accepted November 17, 2016. Date of publication January 4, 2017; date of current version February 8, 2017. The Associate Editor coordinating the review process was Dr. Amitava Chatterjee. *(Corresponding author: S. Pasinetti.)*

S. Pasinetti, I. Bodini, and G. Sansoni are with the Department of Information Engineering, University of Brescia, 25123 Brescia, Italy. (e-mail: simone.pasinetti@unibs.it).

M. Lancini and F. Docchio are with the Department of Mechanical and Industrial Engineering, University of Brescia, 25123 Brescia, Italy.

Digital Object Identifier 10.1109/TIM.2016.2635999

lenses. This technology is gaining increased attention in many fields, due to the ability to vary the camera lens focal length without moving any part [21], [22]. Hence, compact, robust, and miniaturized systems can be designed, suitable for a number of applications such as confocal microscopy [23], vibrometry [24], astronomy [25], medicine [26], [27], and security [28].

In our system, a suitable set of different focal lengths, obtained by properly changing the liquid lens supply voltage, provides multiple camera settings without duplicating the system elements or using moving parts. For each camera setting, a single contrast curve is obtained over the corresponding depth range. A suitable combination of multiple contrast curves is proposed to extend the measurement range and to improve the measurement performances with respect to the state of the art. In particular, two measurement methods were designed: the former, called intensity contrast method (ICM), uses at least two contrast curves covering two adjacent depth subranges and measures the depth information based on the intensity values of the contrast. The latter, called differential contrast method (DCM), uses the contrast curves in pairs and combines each pair in a single differential function; the availability of multiple contrast curves allows defining a suitable number of differential functions, each covering adjacent depth ranges; the depth measurement is carried out using the values of these differential functions.

The research activity focused on the design of the coaxial system optical layout, the characterization of the variable focus objective used in the system, the implementation of the MMP method as presented in [15] and [16] for the achievement of the contrast curves, the calibration of the system to obtain the relation between the contrast focus-dependent curves versus the depth information, the implementation of both ICM and DCM methods, and the experimental characterization of the system measurement performances.

II. Measurement Principle

The measurement principle is based on the estimation of the blur level of the acquired image. The defocus principle is shown in Fig. 1, where the thin lens approximation is considered.

Point $P_1(x_P, y_P)$ is an object point at distance S_{P1} from the lens L, having a focal length F. Its conjugate in-focus point $P'(i_P, j_P)$ on the image plane is located at distance U from the lens, according to the well-known lens maker equation

$$\frac{1}{F} = \frac{1}{S_{P1}} + \frac{1}{U}. \tag{1}$$

When P_1 moves to P, at distance S_P from L, its image at distance U blurs in a circle of confusion of diameter d. Using the optical geometry and (1), diameter d can be expressed as a function of the system parameters [29]

$$d = U \cdot D \cdot \left(\frac{1}{F} - \frac{1}{S_P} - \frac{1}{U}\right) \tag{2}$$

where D is the lens diameter.

The intensity distribution within the blur circle can be described by a point-spread function h. Taking into account the effects of diffraction, chromatic aberration, and other effects, h is usually approximated by a 2-D Gaussian function [30]

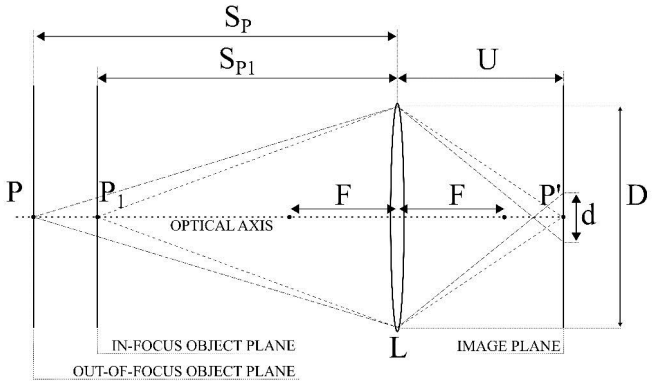

Fig. 1. Defocus principle: geometry of the image formation.

$$h(i,\ j) = \frac{1}{2\pi \cdot \sigma^2} \exp\left(-\frac{i^2 + j^2}{2 \cdot \sigma^2}\right) \tag{3}$$

where *(i, j)* are the image plane coordinates relative to the circle of confusion center, and σ is the spread parameter, directly proportional to the circle of confusion diameter d

$$\sigma = k \cdot d. \tag{4}$$

The proportionality constant k in (4) is characteristic of the optical system and is determined by an appropriate calibration procedure [31]. Thus, the combination of (4) and (2) yields the measurement of depth S_P. To measure σ, we use an active method based on MMP [32]. If a sinusoidal pattern is projected on the scene, the in-focus light intensity distribution $I_f(i, j)$ at the image plane can be expressed as follows:

$$I_f(i,\ j) = I_0(i,\ j) \cdot B(i,\ j) \cdot \{1 + C_0(i,\ j) \cdot \cos[\omega_U \cdot i + \varphi_0(i,\ j)]\}. \tag{5}$$

In (5), $I_0(i, j)$ is the background intensity, $B(i, j)$ is the surface brightness, $C_0(i, j)$ is the in-focus contrast of the projected fringes, ω_U is the fringe frequency at the image plane, and $\phi_0(i, j)$ is the fringe phase. The out-of-focus light intensity distribution $I_d(i, j)$ can be expressed by the convolution between $I_f(i, j)$ and $h(i, j)$ as [30]

$$I_d(i,\ j) = I_f(i,\ j) * h(i,\ j). \tag{6}$$

Inserting expressions (5) and (3) into (6), the defocused image $I_d(i, j)$ results

$$I_d(i,\ j) = I_0(i,\ j) \cdot B(i,\ j) \cdot \{1 + C(i,\ j) \cdot \cos[\omega_U \cdot i + \varphi_0(i,\ j)]\} \tag{7}$$

where $C(i, j)$ is the fringe contrast map defined as

$$C(i,\ j) = C_0(i,\ j) \cdot e^{-\frac{1}{2} \cdot \left(\frac{\omega_U}{2\pi}\right)^2 \cdot \sigma^2}. \tag{8}$$

From (8), we note that the contrast map $C(i, j)$ depends on diameter d: the measurement of depth S_P is therefore possible by measuring $C(i_P, j_P)$.

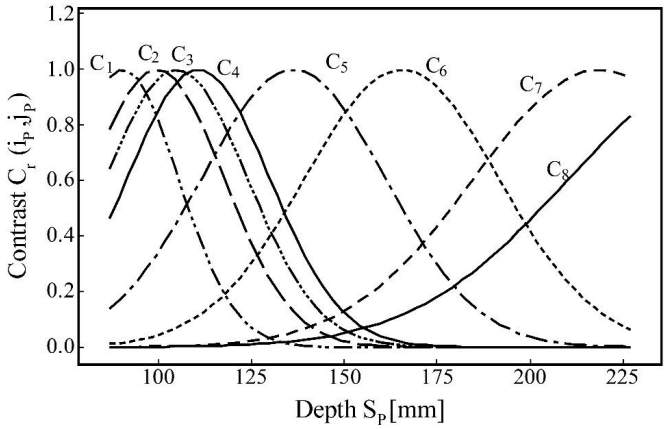

Fig. 2. Contrast $C_r(i_P, j_P)$ as a function of depth S_P, for different values F_r of the focal length F. C_1: $F_1 = 13.60$ mm; C_2: $F_2 = 13.79$ mm; C_3: $F_3 = 13.88$ mm; C_4: $F_4 = 13.98$ mm; C_5: $F_5 = 14.29$ mm; C_6: $F_6 = 14.60$ mm; C_7: $F_7 = 14.93$ mm; and C_8: $F_8 = 15.05$ mm.

A well-established method to measure the contrast map of an image is the phase-shift technique [33], where a sinusoidal pattern is shifted in phase by N times and projected on the object; each corresponding image $I_{d,n}$ is acquired and the contrast map is computed as in (9), as shown at the bottom of this page. In our case, N equals 4.

A normalization procedure consisting of adding two additional images to the above projection sequence (an all-white image and an all-black image) is used as in [34]. Through background subtraction and normalization, it is possible to enhance the gray levels of the acquired images without affecting the contrast, and to compensate for the background illumination and nonuniform object reflection.

Given a generic object point P, the relation between $C(i_P, j_P)$ and S_P is not monotonic: in fact, each value $C(i_P, j_P)$ corresponds to two different values of depth S_P, one corresponding to a position in front of the in-focus object plane, and the other behind it. This introduces an ambiguity problem in the depth evaluation from contrast values. A possible solution is to use only one of the two sides of the curve, but this results in a short measurement range. To extend the range, different system layouts were proposed [30], [35], [36]. All the layouts lead to two different contrast curves (each one covering different depth ranges): the monotonic part of each one is used for the depth measurement, thereby extending the range at the expense of an increased system complexity.

In our approach, the use of a variable focus objective allows to extend the measurement range, maintaining, at the same time, a simple optical configuration. A possible set of $C_r(i_P, j_P)$ curves, obtained from (8), with different values F_r of the focal length F, is depicted in Fig. 2.

In the figure, we note that the peak of the curves moves toward increasing depths as the focal length F_r increases. In addition, higher F_r values result in increased curve widths (i.e., higher depths of field).

Extending the depth range with the aid of the set of C_r curves in Fig. 2 requires the following: 1) the monotonicity of each curve in the selected range and 2) a sufficiently high slope of each curve to ensure adequate measurement sensitivity. The choice of an appropriate slope is a tradeoff between the measurement sensitivity and the measurement range: the higher the slope of a contrast curve, the higher the sensitivity, but the lower the depth range covered. As an example, curves C_1 and C_7 in Fig. 2 fulfill these requirements, allowing unambiguous measurements over a range from 90 to 219 mm (i.e., the positions of the curve maxima). This method, which uses the C_r curves "per se," was defined as *"Intensity Contrast Method"* (ICM).

Another method, alternative to ICM, consists in introducing an additional set of curves, derived from the C_r curves, defined as follows:

$$Q_l^m = \frac{C_l - C_m}{C_l + C_m}. \tag{10}$$

In (10), C_l and C_m are any pair of curves among the C_r curves in Fig. 2. Q_l^m, by definition, are monotonic: their value ranges between -1 and $+1$, being zero when C_l and C_m have the same nonzero value, and ± 1 when one of them is zero. Fig. 3 shows a set of Q_l^m curves. From the figure, it is evident how the curve Q_6^5 obtained by combining C_6 and C_5, could, alone, cover the entire measurement range from 87 to 227 mm. In fact, beyond being monotonic, it does not saturate. However, its slope is not optimal for high sensitivity measurements, except for the central portion. Thus, the combined use of all the four curves was thought to be strategic, to optimize the sensitivity over the whole depth range. Each curve should be used only in its highest slope portion, with the assumption that each couple of neighboring curves is overlapped. The measurement method based on the use of the Q_l^m curves was defined as *"Differential Contrast Method"* (DCM).

In the following section, we present the optical layout of the measurement system, and discuss the ICM and DCM measurement approaches.

III. Experimental Setup

A. Optical Layout

The optical layout of the whole system is shown in Fig. 4. It consists of a projection system and of an acquisition system. The former is an LCD projector equipped with a telecentric objective. The LCD generates Ronchi fringes at a spatial frequency ω_S used in the phase-shift procedure, according to (9).

$$C(i,\ j) = \frac{2 \cdot \sqrt{\left[\sum_{n=0}^{n=N-1} I_{d,n}(i,\ j) \cdot \sin\left(\frac{2\pi \cdot n}{N}\right)\right]^2 + \left[\sum_{n=0}^{n=N-1} I_{d,n}(i,\ j) \cdot \cos\left(\frac{2\pi \cdot n}{N}\right)\right]^2}}{\sum_{n=0}^{n=N-1} I_{d,n}(i,\ j)} \tag{9}$$

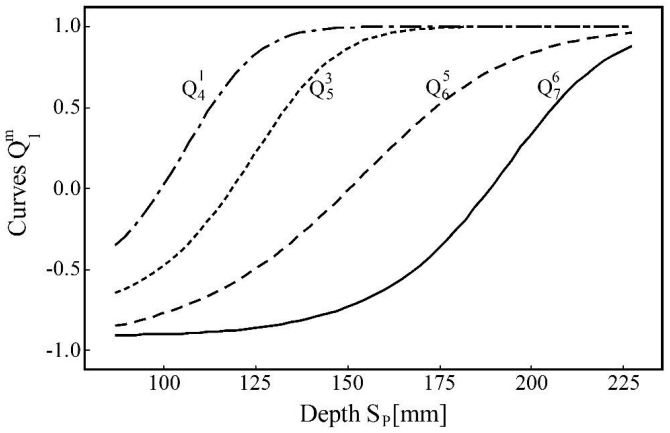

Fig. 3. Set of multiple Q_l^m curves used to measure the object positions using the DCM approach.

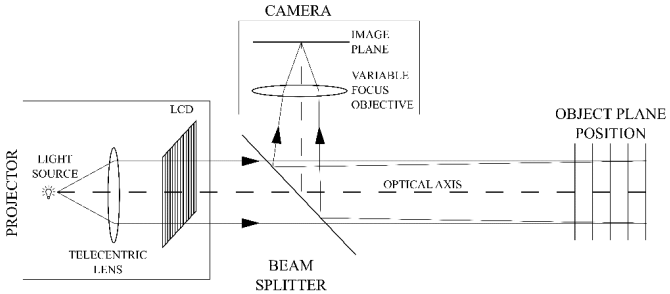

Fig. 4. Optical layout of the system.

The latter is a camera equipped with a variable focus objective: it is an *Ids UI-1540SE*, with a resolution of 1280×1024 pixels and with a pixel size of 5.2 μm. The variable focus objective is a *Varioptic Caspian C-39-N0* with a focal length of 16 mm and a diameter D of 11 mm. It contains a *Varioptic Artic 39N0*, variable-focus liquid lens, with minimum and maximum optical powers of -15 and $+27$ diopters, respectively, controllable by varying its supply voltage from 25 V (minimum optical power) to 70 V (maximum optical power). The *Varioptic Caspian C-39N0-16* is thus a combination of fixed lenses and of the liquid lens *Varioptic Artic 39N0*.

To avoid the typical problems of triangulating systems, such as the presence of occlusions and shadows, the projection and the acquisition sections are made coaxial by means of a beam splitter placed after them. The beam splitter deviates the optical rays projected by the LCD and diffused by the object toward the camera. Due to telecentric projection, the frequency ω_U of the fringes at the image plane depends only on the camera magnification

$$\omega_U = \omega_S \cdot \frac{S_P}{U}. \tag{11}$$

The period of the projected Ronchi fringes is 2 mm, corresponding to $\omega_S = 0.5$ mm^{-1}. This is the minimum fringe period achievable with the projector used in our setup. A higher spatial frequency should further improve the system performances, care being taken for the limits due to the camera image resolution.

The image plane distance U is 16 mm, and the object distance S_P ranges from 87 to 227 mm. To obtain sinusoidal fringes (required for the measurement procedure) from Ronchi fringes, a low-pass filter is applied on the acquired images, with a cutoff frequency optimized to isolate the first harmonic pattern.

B. Implementation of the ICM and DCM Approaches

The ICM and DCM methods were performed in two steps: 1) calibration and 2) measurement. Calibration consists of finding the relation among each object point position S_P, the focal length F, and the contrast curves $C_r(i_P, j_P)$ over the whole measurement range. To this aim, a white target plane was positioned at a known distance from the objective. Then, the objective focal length was set at a given value F_r. Then a series of images was taken by projecting the phase-shifted fringes on the target and the contrast C_r was computed according to (9). The procedure was repeated for a suitable number of focal lengths, by varying the liquid lens voltage control. The position of the plane was then changed to cover the whole measurement range at equal steps, and the above procedure was repeated at each position. As a result of this first step, a set of calibration C_r curves was obtained. Using the criteria described in Section II, suitable combinations of C_r and Q_l^m curves were selected for the ICM and the DCM approaches, respectively.

The measurement step consists in the evaluation of the unknown object position S_P using the information derived from calibration. To this aim, the objective focal length F was set to each *selected* value F_r, the phase-shifted pattern sequence was projected on the object, and the corresponding measured contrast $C_{r,\text{meas}}(i_P, j_P)$ was computed according to (9). In the ICM method, the corresponding calibration C_r curve was inverted and the depth S_P was retrieved by evaluating it for $C_r = C_{r,\text{meas}}$; in the DCM method, $Q_{l,\text{meas}}^m$ was computed and the corresponding calibration Q_l^m curve was inverted and evaluated for $Q_l^m = Q_{l,\text{meas}}^m$.

IV. Experimental Results

A. Characterization of the CASPIAN C-39N0-16 Module

To accurately determine the relation between the applied voltage and the optical power of the objective, the objective-camera combination was initially characterized. For this purpose, the following iterative procedure was performed. A plane perpendicular to the optical axis was set at a given distance from the objective, and the corresponding image was acquired by the camera. The focal length F, required to focus the image, was computed using (1). The procedure was repeated for a convenient number of positions of the object plane ranging from 87 to 227 mm in steps of 10 mm. The value of U in (1) was 16 mm.

The results of the characterization procedure are shown in Fig. 5: the values of the optical power OP (left vertical scale) and of the focal length F (right vertical scale) are displayed as a function of the voltage applied to the liquid lens (lower horizontal scale) and of the position of the target plane (upper horizontal scale).

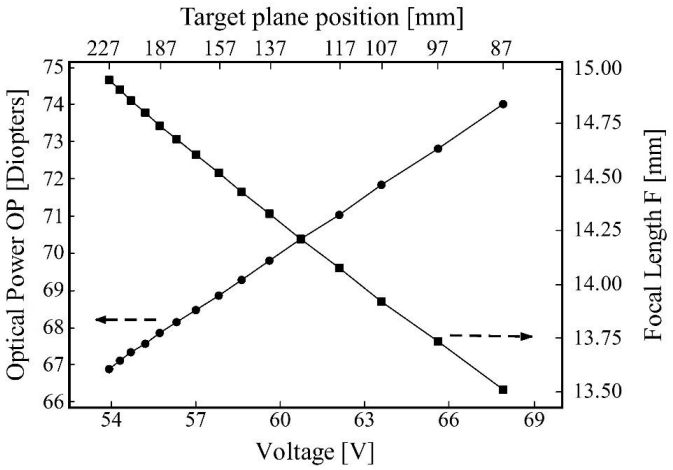

Fig. 5. Plot of the optical power *OP* (left vertical scale) and of the optical focal length F (right vertical scale) of the C-39N0-16 as a function of the voltage range (lower horizontal scale) and of the position of the target plane (upper horizontal scale). Dashed arrows indicate the reference vertical axis of each line.

From the figure, we note that both *OP* and F curves are fairly linear throughout the voltage range, the relation between the applied voltage and the optical power being

$$\text{OP} = m \cdot \text{Voltage} + q \tag{12}$$

where $m = 50.52 \times 10^{-2}$ diopters/V and $q = 39.69$ diopters.

B. Calibration Procedure

The calibration procedure is aimed at deriving the C_r curves at known S_P positions. As an example, Fig. 6(a) shows the experimental contrast values evaluated at image point (100, 100), for $S_P = 159.5$ mm, each value belonging to a specific C_r curve for focal lengths F_r from 13.32 to 15.40 mm and at steps corresponding to voltage variations of 1 V.

Fig. 6(b) shows three sample images of a fringe pattern, taken at focal lengths $F_1 = 14.08$, $F_2 = 14.49$, and $F_3 = 14.71$ mm, and corresponding to positions 1, 2, and 3 in Fig. 6(a). Position 2 represents the in-focus condition, whereas positions 1 and 3 represent two out-of-focus conditions.

The acquisition of C_r values over the entire depth range from 87 to 227 mm, in steps of 2.5 mm results in a large set of calibration curves. A subset of them is illustrated in Fig. 7, for the same values F_r of focal length F used to calculate the theoretical curves of Fig. 2. Increasing the focal length, the curve width increases (i.e., the depth of field increases), as expected. Theoretical and experimental curves fit for a value of the parameter k in (4) equal to 1.06, with the following differences: 1) the decreasing peak values of the experimental curves at increasing F_r values (due to the nontelecentric nature of the camera lens) and 2) the presence of noise in the measured contrast, which is particularly critical for low-contrast values [37].

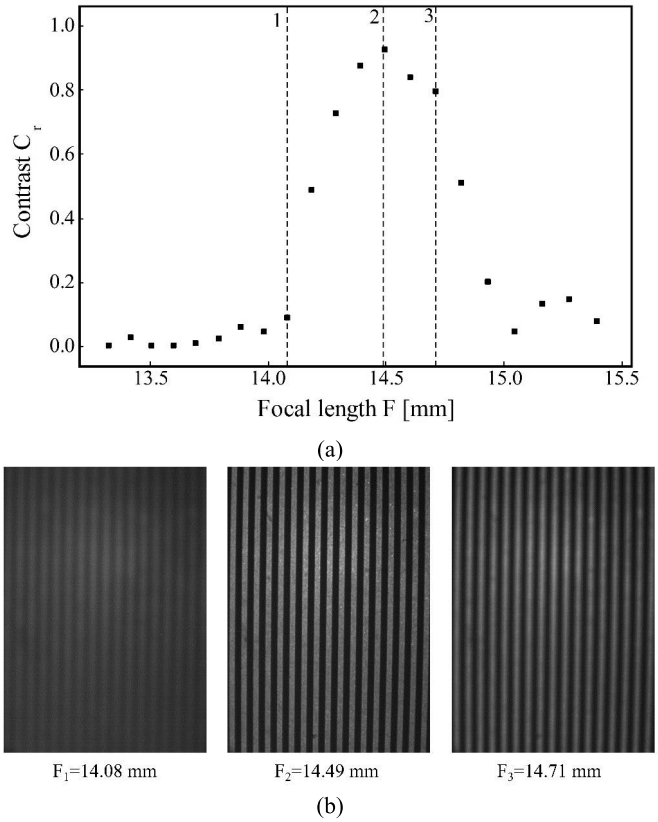

Fig. 6. Calibration procedure. (a) Experimental contrast values C_r at image point (100, 100), for $S_P = 159.5$ mm, as a function of the focal length F. (b) Images of the projected fringes acquired by the camera at different values F_r of focal length F.

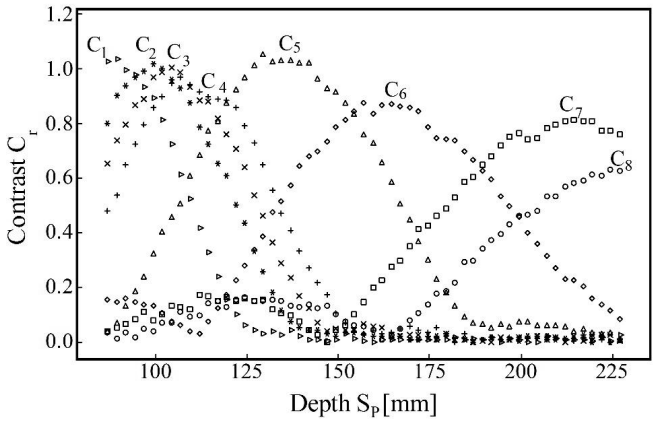

Fig. 7. Experimental values of the contrast C_r as a function of S_P for different values F_r of F. C_1: $F_1 = 13.60$ mm; C_2: $F_2 = 13.79$ mm; C_3: $F_3 = 13.88$ mm; C_4: $F_4 = 13.98$ mm; C_5: $F_5 = 14.29$ mm; C_6: $F_6 = 14.60$ mm; C_7: $F_7 = 14.93$ mm; and C_8: $F_8 = 15.05$ mm.

C. ICM Experimental Approach

The requirements to obtain a pair of curves to be used for unambiguous evaluation of the distance from contrast curves using ICM were described in Section II. We applied these requirements for the set of experimental curves of Fig. 7. As already stated, a difference between the experimental and theoretical curves is the presence of noise. To avoid it,

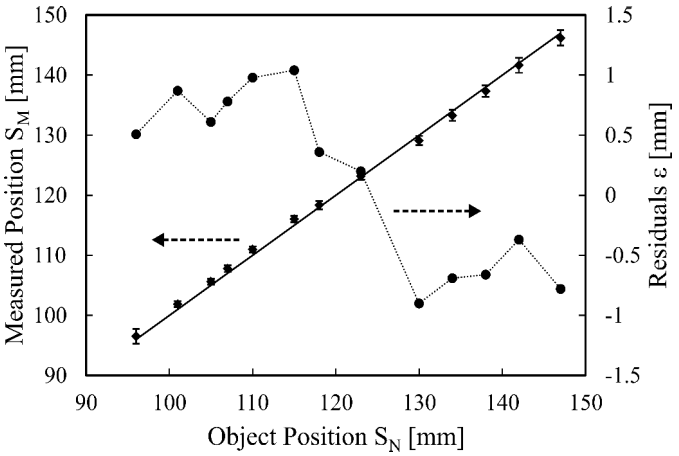

Fig. 8. Plot of the mean values of the measured positions S_M (♦ symbols, left vertical scale) with their standard deviations (bars), and of the corresponding residuals ε (• symbols, dashed line, right vertical scale) as a function of the nominal object position S_N, resulting from the ICM approach. The solid line is the bisecting line. Dashed arrows indicate the reference vertical axis of each line.

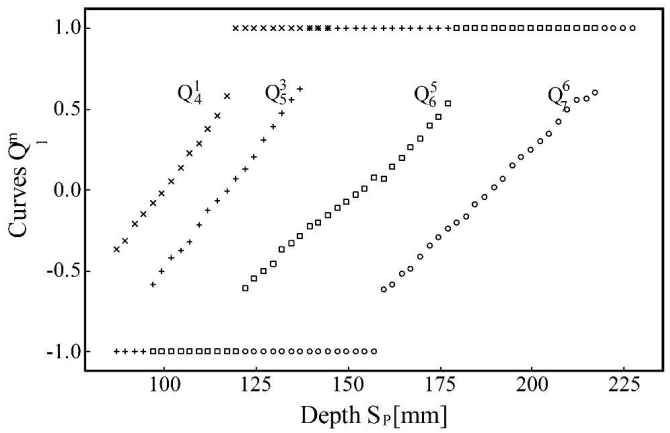

Fig. 9. Set of the experimental Q_l^m curves used to measure the object positions using the DCM approach. $F_1 = 13.60$ mm; $F_3 = 13.88$ mm; $F_4 = 13.98$ mm; $F_5 = 14.29$ mm; $F_6 = 14.60$ mm; and $F_7 = 14.93$ mm.

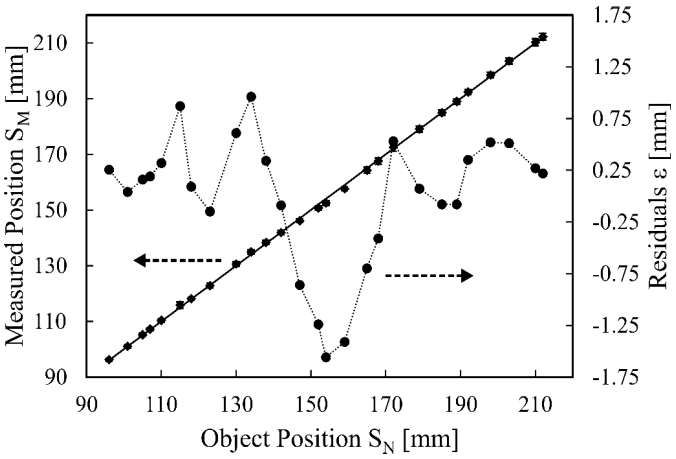

Fig. 10. Plot of the mean values of the measured positions S_M (♦ symbols, left vertical scale) with their standard deviations (bars), and of the residuals ε (• symbols, dashed line, right vertical scale) as a function of the nominal object position S_N, resulting from the DCM approach. The solid line is the bisecting line. Dashed arrows indicate the reference vertical axis of each line.

a threshold contrast value is required (in our case we used a threshold of 0.18). The insertion of a threshold results in the possibility that two curves above threshold do not entirely overlap. A further requirement is necessary in addition to the two discussed in Section II, i.e., each curve pair should be at least partially overlapped *above the selected contrast threshold* to avoid *"holes"* in the depth range. Referring to Fig. 7 again, the curve pair overlapping at contrast values $C_r > 0.18$ is represented by curves C_1 and C_6, corresponding to a depth range from 90 mm (peak position of C_1) to 155 mm (peak position of C_6).

For each image point, depth measurement was carried out by applying the measurement procedure described in Section II for F_1 and F_6. Depth values S_P were evaluated only for image points corresponding to measured contrast values greater than the threshold. Two depth maps $S_1(i, j)$ and $S_6(i, j)$ were obtained, complementary to each other, with the exception of points (i, j), where both $C_1(i, j)$ and $C_6(i, j)$ were above threshold. In these cases, the mean value between the elements in the two maps was taken as the estimate of depth.

1) ICM Performances: The measurement performances were evaluated using a plane surface mounted on an automatically controlled slit oriented along the system optical axis, and evaluating depth maps S_1 and S_6 at known positions S_N in the selected depth range. The results are shown in Fig. 8, where full diamonds and bars (left vertical scale) represent the average S_M values with their standard deviations, as a function of the known S_N values. Full dots (right vertical scale) represent the residuals ε, i.e., the differences between the means of the measured points and the nominal object plane position. The solid line is the bisecting line. The residuals have a pivot-like trend with respect to an object position of about 123 mm. This is certainly attributable to underestimation of the results (before the pivot, where C_1 curve is used) and overestimation of the results (after the pivot, where curve C_6 is used).

The σ_0 of the ICM method was computed with a linear regression on all the measured points. The linearity of the measurements over the selected range is excellent ($R^2 = 0.9994$) and the results of $\sigma_0 = 0.55$ mm over a depth range of about 60 mm, which corresponds to the 0.92 % of the range, are very encouraging, being comparable with the state-of-the-art DFD systems.

D. DCM Experimental Approach

The application of the two criteria stated in Section II (derived from a theoretical standpoint) and the third criteria introduced in the previous section (due to the insertion of a contrast threshold) results in the choice of the curves Q_l^m shown in Fig. 9; these are computed by combining the contrast curves in Fig. 7. Comparing Figs. 3 and 9 shows that, in the experimental situation, curves Q_l^m present abrupt discontinuities due to the contrast threshold used to avoid noise contribution. This behavior is not critical for the choice of the

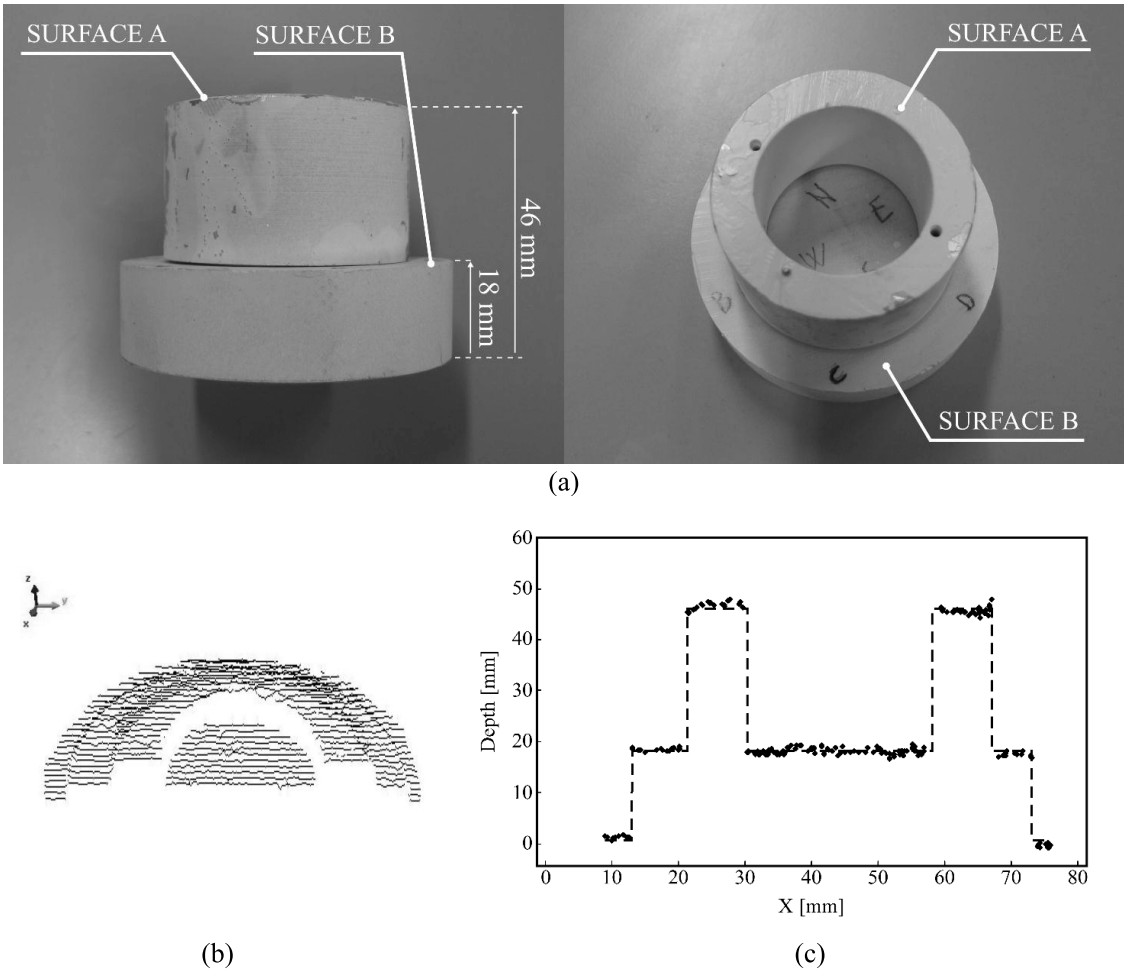

Fig. 11. Measurement results from a sample bicylindrical object used to demonstrate the system performance using DCM. (a) Images of the object. (b) 3-D reconstruction. (c) Depth profile of a single section as a function of the lateral dimension (the dashed line represents the real object).

measurement range, as four curves can be used to extend the depth range from 87 to 222 mm.

The depth measurement was carried out for each image point by applying the measurement procedure described in Section II for F_1, F_3, F_4, F_5, F_6, and F_7. Four depth maps were obtained, namely, S_4^1, S_5^3, S_6^5, and S_7^6, the depth of each point *(i, j)* being computed in at least one map. The average over corresponding values in the four maps was taken as the measurement of the depth of point *(i, j)*.

1) DCM Performances: The measurement performances of DCM were evaluated with the same experimental setup used for the ICM method. The results are shown in Fig. 10: full diamonds (left vertical scale) and bars represent the average S_M values with their standard deviations, as a function of known S_N values. Full dots (right vertical scale) represent the residuals ε, i.e., the difference between the mean of the measured points at each object plane position, and its nominal position. Again, the solid line is the bisecting line. Compared to the residuals in Fig. 8, here the residuals are uniform in the whole measurement range, apart from a negative peak around $S_N = 155$ mm. This is explainable, in the present setup, by observing curve Q_6^5 in Fig. 9. Indeed this curve is the most irregular of the set of Q-Curves, with a small dip corresponding to the point of maximum residual value.

σ_0 was computed as in the ICM method, i.e., with a linear regression over all the measured points. As in the ICM, the results obtained with the DCM method show excellent linearity over the whole measurement range ($R^2 = 0.9997$). The DCM method resulted in $\sigma_0 = 0.76$ mm over a depth range of about 135 mm, which corresponds to the 0.56 % of the range. Even if, with the DCM method, σ_0 slightly increases with respect to the ICM method, there is a much higher benefit from the increase in the depth range, which is more than twice as large as in ICM. Theoretically, the measurement range of the DCM method can be expanded at will, selecting the liquid lens focal lengths, within the limit of telecentric projection.

A real object measured with the DCM method is shown in Fig. 11(a). A concentric bicylindrical object, composed of a filled baseline and a superimposed hollow cylinder, was used. Depth dimensions were 18 mm for the baseline, and 28 mm for the hollow cylinder. The object was placed at different positions within the measurement range of Fig. 9. The object was almost orthogonal to the optical axis. Fig. 11(b) shows a 3-D measurement of the object, placed so that its baseline corresponded to 207 mm from the lens, processed using curves

TABLE I

MEAN AND STANDARD DEVIATION OF THE MEASURED DEPTHS OF EACH FLAT SURFACE OF THE OBJECT IN FIG. 11, COMPUTED FROM MULTIPLE MEASUREMENTS OF THE SAME SECTION (ROWS), WITH THE OBJECT PLACED IN DIFFERENT POSITIONS WITHIN THE MEASUREMENT RANGE (COLUMNS)

# of meas.	Baseline = 207 mm		Baseline = 187 mm		Baseline = 167 mm	
	Surface A [mm]	Surface B [mm]	Surface A [mm]	Surface B [mm]	Surface A [mm]	Surface B [mm]
1	18.66±0.78	46.19±0.56	18.52±0.65	46.59±0.74	18.54±0.78	46.62±0.73
2	18.70±0.76	46.10±0.60	18.47±0.68	46.61±0.72	18.59±0.74	46.66±0.76
3	18.74±0.65	46.15±0.72	18.48±0.73	46.57±0.77	18.61±0.77	46.65±0.75
4	18.70±0.75	46.19±0.65	18.43±0.66	46.55±0.78	18.56±0.79	46.63±0.74
5	18.55±0.79	46.17±0.50	18.55±0.73	46.56±0.74	18.55±0.79	46.60±0.76

Q_6^5 and Q_7^6 in Fig. 9, and reconstructed using the Software Polyworks. Fig. 11(c) shows the profile of a single section, as a function of its lateral dimension.

Repeated measurements on the same section of the object, with the object placed at arbitrary positions within the measurement range, yielded the results shown in Table I. The depth values for both the surfaces resulted to be consistent with the nominal values.

It is worth noting that all the measurements shown have been taken using a test-bench object, i.e., a bicylinder, with well-defined upper and lower surfaces. Measurements were performed by keeping the object axis quasi parallel to the optical axis. The performance of the system resulted as described for angles up to $\pm 10°$. Beyond these limits, the residuals increased slightly for the lower plane because of the shadowing caused by the straight cylinder walls. Objects with soft surfaces performed quite the same irrespective of their orientation in space.

V. CONCLUSION

This paper is a contribution to the method of DFD, which benefits from the presence on the market of modern optical imaging components. We presented a compact and versatile system able to perform measurement equal, if not better, than the state of the art, over a depth range much wider than those reported so far in the literature. The system, with telecentric illumination projection and a variable focus objective by means of a liquid lens provides all-in-focus projection and, together with a normalization procedure, avoided problems due to nonuniform illumination and reflection of the measured object. The depth range obtainable could be increased with respect to the traditional DFD systems using the liquid lens objective, the limits being set only by the telecentric illumination. This was achieved with a simple, compact, and easy controllable setup without moving parts.

To process the images we developed two different measurement methods: the former (ICM) uses the contrast curves "per se" to recover the depth information while the latter (DCM) uses a differential combination between pairs of contrast curves. The results obtained were satisfactory with both ICM and DCM: the former yielded a σ_0 of 0.55 mm over a depth range of 60 mm (0.92% of the range); the latter yielded a σ_0 of 0.76 mm over a depth range of 135 mm (0.56% of the range). Both the methods provided excellent linearity and negligible systematic errors, in line or better, with respect to the state of the art in the DFD measurement; however, the DCM method resulted in a much higher depth range than the existing systems in the literature.

The limitations of the setup, in the present version, are an increase in the measurement residuals for objects with sharp edges for inclinations above $\pm 10°$, and the somewhat arbitrary choice of the Q-Curves to be used in the DCM method. We are actually working to fix the former limitation by means of additional image elaboration algorithms, and the latter limitation by using an optimization routine able to optimize the choice of the Q-curves to automate the measurement.

REFERENCES

[1] R. Anchini, G. Di Leo, C. Liguori, and A. Paolillo, "Metrological characterization of a vision-based measurement system for the online inspection of automotive rubber profile," *IEEE Trans. Instrum. Meas.*, vol. 58, no. 1, pp. 4–13, Jan. 2009.

[2] E. Lilienblum and A. Al-Hamadi, "A structured light approach for 3-D surface reconstruction with a stereo line-scan system," *IEEE Trans. Instrum. Meas.*, vol. 64, no. 5, pp. 1258–1266, May 2015.

[3] R. Anchini, G. Di Leo, C. Liguori, and A. Paolillo, "A new calibration procedure for 3-D shape measurement system based on phase-shifting projected fringe profilometry," *IEEE Trans. Instrum. Meas.*, vol. 58, no. 5, pp. 1291–1298, May 2009.

[4] G. Sansoni, M. Trebeschi, and F. Docchio, "State-of-the-art and applications of 3D imaging sensors in industry, cultural heritage, medicine, and criminal investigation," *Sensors*, vol. 9, no. 1, pp. 568–601, Jan. 2009.

[5] G. Tognola, M. Parazzini, P. Ravazzani, F. Grandori, and C. Svelto, "3-D acquisition and quantitative measurements of anatomical parts by optical scanning and image reconstruction from unorganized range data," *IEEE Trans. Instrum. Meas.*, vol. 52, no. 5, pp. 1665–1673, Oct. 2003.

[6] G. Di Leo, C. Liguori, and A. Paolillo, "Covariance propagation for the uncertainty estimation in stereo vision," *IEEE Trans. Instrum. Meas.*, vol. 60, no. 5, pp. 1664–1673, May 2011.

[7] G. Sansoni, P. Bellandi, and F. Docchio, "3D system for the measurement of tube eccentricity: An improved, rugged, easy to calibrate layout," *Meas. Sci. Technol.*, vol. 24, no. 3, pp. 1–11, 2013.

[8] T. P. Pachidis and J. N. Lygouras, "Pseudostereo-vision system: A monocular stereo-vision system as a sensor for real-time robot applications," *IEEE Trans. Instrum. Meas.*, vol. 56, no. 6, pp. 2547–2560, Dec. 2007.

[9] S. Zhu and Y. Gao, "Noncontact 3-D coordinate measurement of cross-cutting feature points on the surface of a large-scale workpiece based on the machine vision method," *IEEE Trans. Instrum. Meas.*, vol. 59, no. 7, pp. 1874–1887, Jul. 2010.

[10] S. W. Bailey, J. I. Echevarria, B. Bodenheimer, and D. Gutierrez, "Fast depth from defocus from focal stacks," *Vis. Comput.*, vol. 31, no. 12, pp. 1697–1708, Dec. 2015.

[11] Y. Y. Schechner and N. Kiryati, "Depth from defocus vs. stereo: How different really are they?" *Int. J. Comput. Vis.*, vol. 39, no. 2, pp. 141–162, Sep. 2000.

[12] P. Trouvé, F. Champagnat, G. Le Besnerais, J. Sabater, T. Avignon, and J. Idier, "Passive depth estimation using chromatic aberration and a depth from defocus approach," *Appl. Opt.*, vol. 52, no. 29, pp. 7152–7164, Oct. 2013.

[13] V. P. Namboodiri and S. Chaudhuri, "On defocus, diffusion and depth estimation," *Pattern Recognit. Lett.*, vol. 28, no. 3, pp. 311–319, Feb. 2007.

[14] B. Girod and S. Scherock, "Depth from defocus of structured light," *Proc. SPIE*, vol. 1194, pp. 209–215, Apr. 1990.

[15] Y. Otani, F. Kobayashi, Y. Mizutani, S. Watanabe, M. Harada, and T. Yoshizawa, "Uni-axial measurement of three-dimensional surface profile by liquid crystal digital shifter," *Proc. SPIE*, vol. 7790, p. 77900A, Aug. 2010.

[16] Y. Dou and X. Su, "A flexible 3D profilometry based on fringe contrast analysis," *Opt. Laser Eng.*, vol. 44, no. 4, pp. 844–849, Jun. 2012.

[17] T. Yoshizawa, T. Shinoda, and Y. Otani, "Uniaxis rangefinder using contrast detection of a projected pattern," *Proc. SPIE*, vol. 4190, pp. 115–122, Feb. 2001.

[18] Y. Dou, X. Su, Y. Chen, and Y. Wang, "A flexible fast 3D profilometry based on modulation measurement," *Opt. Laser Eng.*, vol. 49, no. 3, pp. 376–383, Mar. 2011.

[19] Y. Wang, X. Su, and Y. Dou, "A fast three-dimensional object recognition based on modulation analysis," *Opt. Laser Eng.*, vol. 48, no. 10, pp. 1027–1033, Oct. 2010.

[20] H. Zhipan, L. Zhenzhong, W. Qiufeng, and F. Lifang, "A novel approach to recovering depth from defocus," *Sensors Transducers*, vol. 160, no. 12, pp. 36–41, Dec. 2013.

[21] S. Casutt, M. Bueeler, M. Blum, and M. Aschwanden, "Fast and precise continuous focusing with focus tunable lenses," *Proc. SPIE*, vol. 8982, p. 89820Y, Mar. 2014.

[22] J. Fuentez-Fernández, S. Cuevas, L. C. Alvarez-Nuñez, and A. Watson, "Tests and evaluation of a variable focus liquid lens for curvature wavefront sensors in astronomy," *Appl. Opt.*, vol. 52, no. 30, pp. 7256–7264, Oct. 2013.

[23] T. Yang, L. Wang, and H. Duan, "Optical design used in Z-stack imaging based on liquid lens," *Proc. SPIE*, vol. 7849, p. 78492R, Nov. 2010.

[24] R. Atashkhooei, U. Zabit, S. Royo, T. Bosch, and F. Bony, "Adaptive optical head for industrial vibrometry applications," *Proc. SPIE*, vol. 8082, p. 80821W, May 2011.

[25] J. Fuentez-Fernández, S. Cuevas, L. C. Alvarez-Nuñez, and A. M. Watson, "Applications of variable focus liquid lenses for curvature wave-front sensors in astronomy," *Proc. SPIE*, vol. 9148, p. 91485J, Aug. 2014.

[26] L. Wang, A. Cassinelli, H. Oku, and M. Ishikawa, "A pair of diopter-adjustable eyeglasses for presbyopia correction," *Proc. SPIE*, vol. 9193, p. 91931G, Sep. 2014.

[27] S. Lee, M. Choi, E. Lee, K.-D. Jung, J.-H. Chang, and W. Kim, "Four zoom lens design for 3D laparoscope by using liquid lens," *Proc. SPIE*, vol. 8488, p. 848809, Oct. 2012.

[28] C. W. Tsai, P. J. Wang, and J. A. Yeh, "Compact touchless fingerprint reader based on digital variable-focus liquid lens," *Proc. SPIE*, vol. 9193, p. 91930M, Sep. 2014.

[29] S. Chaudhuri and A. N. Rajagopalan, "Depth recovery from defocused images," in *Depth From Defocus: A Real Aperture Imaging Approach*. New York, NY, USA: Springer-Verlag, 1999, pp. 14–27.

[30] A. Horii, "Depth from defocusing," Comput. Vis. Active Perception Lab., Royal Inst. Technol., Stockholm, Sweden, Tech. Rep., 1992

[31] M. Subbarao and N. Gurumoorthy, "Depth recovery from blurred edges," in *Proc. CVPR*, Jun. 1988, pp. 498–503.

[32] L. Su, X. Su, W. Li, and L. Xiang, "Application of modulation measurement profilometry to objects with surface holes," *Appl. Opt.*, vol. 38, no. 7, pp. 1153–1157, Mar. 1999.

[33] D. Malacara, "Phase shifting intererometry," in *Optical Shop Testing*, 3rd ed. Hoboken, NJ, USA: Wiley, Jul. 2007, pp. 547–666.

[34] G. Sansoni, M. Trebeschi, and F. Docchio, "Fast 3D profilometer based upon the projection of a single fringe pattern and absolute calibration," *Meas. Sci. Technol.*, vol. 17, pp. 1757–1766, Jun. 2006.

[35] C. Zhou, S. Lin, and S. Nayar, "Coded aperture pairs for depth from defocus," in *Proc. ICCV*, Kyoto, Japan, Sep./Oct. 2009, pp. 325–332.

[36] D. Gray, "A single lens with no moving parts for rapid high-resolution 3D image capture," *Proc. SPIE*, vol. 8659, p. 86590N, Feb. 2013.

[37] X. Xin *et al.*, "A comparison of contrast measurements in passive autofocus systems for low contrast images," *Multimedia Tools Appl.*, vol. 69, no. 1, pp. 139–156, Mar. 2014.

Simone Pasinetti received the B.S. degree and the M.S. degree (with Hons.) in automation engineering, and the Ph.D. degree in applied mechanics from the University of Brescia, Brescia, Italy, in 2009, 2011, and 2015, respectively. His master thesis focused on the control of mechanical actuators with SEMG signals. His Ph.D. thesis titled "Development of measurement protocols for the analysis of the functional evaluation and rehabilitation, in biomechanics field."

He was with the Institute of Intelligent Systems and Robotics, Paris, France, during the Ph.D, where he was involved in researches on the dynamic posture analysis. Since 2015, he has been a Research Fellow with the Optoelectronics Laboratory, Department of Information Engineering, University of Brescia. He is currently involved in posture analysis, liquid lens objectives applications, and 3-D vision systems development. His current research interests include the biomechanics of human posture, EMG analysis, and 2-D and 3-D vision systems.

Ileana Bodini received the master's degree in mechanical engineering and the Ph.D. degree from the University of Padua, Padua, Italy, in 2006 and 2010, respectively.

From 2007 to 2009, she attended the Ph.D. School of Research in Sciences, Technologies, and Measurements for Space-Mechanical Measurement for Engineering, University of Padua. Since 2007, she has been with the Group of Mechanical and Thermal Measurement, University of Brescia, Brescia, Italy, where she has been with the Laboratory of Optoelectronics, since 2014. Her current research interests include the design and dimensioning of 2-D and 3-D vision (embedded and nonembedded) systems for research and industrial application, the development of measurement devices based on vision systems, and the techniques for industrial measurements and diagnostic based on vision systems and image processing.

Matteo Lancini received the master's degree in mechanical engineering and the Ph.D. degree in applied mechanics from the University of Brescia, Brescia, Italy, in 2005 and 2015, respectively.

He was a Research Contractor with the Department of Industrial and Mechanical Engineering, University of Brescia, where he was involved in the development of measurement techniques for industrial diagnostics, and focused on measurements in uncontrolled environments from 2005 to 2009. He is currently an Assistant Professor with the Mechanical and Thermal Measurements Laboratory, Department of Industrial and Mechanical Engineering, University of Brescia. His current research interests include measurement systems for biomechanical analysis, in particular, for robotic gait and rehabilitation, and industrial diagnostics using nondestructive techniques based on vibration measurements.

Dr. Lancini is a member of the International Society of Biomechanics.

Franco Docchio received the M.S. degree in Nuclear Engineering from the Politecnico of Milano, Milan, Italy, in 1976.

He was at the Centro di Elettronica Quantistica, Milan, Italy, between 1978 and 1987, where he carried out research concerning laser development, laser applications in industry and biomedicine, and laser-tissue interaction. In 1987, he joined the Dipartimento di Elettronica per l'Automazione, University of Brescia, Brescia, Italy, where he is currently a Full Professor of Electrical Measurements. He has authored more than 250 publications, mostly international. He is a member of the Laboratory of Optoelectronics, University of Brescia, Brescia, Italy. In recent years, within the activities of the Laboratory, he has been active in the creation and incubation of a number of spin-off companies that operate in the domain of optoelectronics, laser processing of materials, optical sensors, and 3-D vision. He holds five international patents on instrumentation and innovative techniques for electro-optical measurements.

Prof. Docchio is currently a fellow of the European Optical Society. He is the Director of the national journal *Tutto_Misure*.

Giovanna Sansoni received the M.S. degree in Electronic Engineering from the Politecnico of Milano, Milan, Italy, in 1984.

In 1985, she joined the University of Brescia, Brescia, Italy, where she is currently a Full Professor of Electrical Measurements with the Department of Information Engineering. Her current research interests include 3-D vision area, the implementation of camera and projector calibration for the absolute measurement of shape in active stereo vision systems, the development of light coding methods for whole-field optical profilometry, the application of optical instrumentation to the acquisition, and the reverse engineering of free-form surfaces.